

RSC Advances



This is an *Accepted Manuscript*, which has been through the Royal Society of Chemistry peer review process and has been accepted for publication.

Accepted Manuscripts are published online shortly after acceptance, before technical editing, formatting and proof reading. Using this free service, authors can make their results available to the community, in citable form, before we publish the edited article. This *Accepted Manuscript* will be replaced by the edited, formatted and paginated article as soon as this is available.

You can find more information about *Accepted Manuscripts* in the [Information for Authors](#).

Please note that technical editing may introduce minor changes to the text and/or graphics, which may alter content. The journal's standard [Terms & Conditions](#) and the [Ethical guidelines](#) still apply. In no event shall the Royal Society of Chemistry be held responsible for any errors or omissions in this *Accepted Manuscript* or any consequences arising from the use of any information it contains.

**Graphene aerogel-supported and graphene quantum dots-modified
 γ -MnOOH nanotubes as a highly efficient electrocatalyst for oxygen
reduction reaction**

Yisi Liu ^{a, b}, Wenzhang Li ^{a, b *}, Jie Li ^{a, b *}, Haibo Shen ^{a, b}, Yaomin Li ^c, Yang Guo ^d

^a School of Chemistry and Chemical Engineering, Central South University, Changsha
410083 China

^b Key Laboratory of Hunan Province for Metallurgy and Material Processing of Rare
Metals, ChangSha, 410083, China

^c Department of Chemistry, University College London, 20 Gordon Street, London,
WC1H 0AJ, UK

^d Max Planck Institut für Chemische Energiekonversion, Stiftstr. 34-36, D-45470
Mülheim an der Ruhr, Germany

*Corresponding author. Tel.: +86 731 8887 9616; fax: +86 731 8887 9616.

E-mail addresses: liwenzhang@csu.edu.cn, lijieliu@csu.edu.cn

Abstract

In this work, we demonstrate a facile strategy to synthesize a novel three-dimensional (3D) graphene aerogel-supported and graphene quantum dots-modified γ -MnOOH nanotubes as a highly efficient electrocatalyst. The structure, morphology, and chemical composition of γ -MnOOH@GA/GQDs are investigated by X-ray diffraction (XRD) spectroscopy, scanning electron microscopy (SEM), transmission electron microscopy (TEM), Raman spectroscopy, and X-ray photoelectron spectroscopy (XPS). The electrocatalytic activity of catalysts is discussed by cyclic voltammograms (CV), electrochemical impedance spectroscopy (EIS), and rotating disk electrode (RDE) measurements in O₂-saturated 0.1 M KOH electrolyte. The γ -MnOOH@GA/GQDs hybrid exhibits more positive onset potential and half-wave potential, faster charge transfer, lower Tafel slope than that of γ -MnOOH@GA, GA and γ -MnOOH, and mainly undergoes a direct 4e⁻ reaction pathway. Furthermore, its electrocatalytic performance is comparable with the commercial 20 wt.% Pt/C, which is attributed to the unique 3D crumpled porous nanostructure of GA with large specific area and fast electron transport, and the synergic covalent coupling between the γ -MnOOH nanotubes and GA. More importantly, the GQDs structural defects can facilitate the adsorption of oxygen and charge transfer. As a highly efficient surface “sensitizer”, GQDs are modified on the γ -MnOOH surfaces to further boost the electrocatalytic property.

Key words: graphene aerogel; graphene quantum dots; electrocatalyst; oxygen

reduction reaction

1. Introduction

Metal-air batteries have attracted much attention due to their several advantages including abundance in resources, low emissions,^{1,2} portability, high energy density, being light weight,^{3,4} environmental benignity,⁵ and great potential application in modern life.⁶ However, the industrial application of metal-air batteries is limited because of low current density and large overpotential exist in the current cathode.⁷⁻⁹ The main cathode reaction of metal-air batteries is oxygen reduction reaction (ORR). Thus, great efforts have been made to explore stable and highly efficient catalysts for accelerating the inherently sluggish ORR kinetics. Traditionally, platinum (Pt), Ruthenium (Ru) and their alloys are used widely as the best ORR catalysts,^{6,10,11} but the high cost and low abundance of noble-metal-based catalysts hamper the practical application of metal-air battery technologies. Consequently, the development of non-precious metal-based catalysts with high activity and good durability for ORR is a great challenge.

Manganese oxides have been utilized extensively as cathodic catalysts for ORR due to low toxicity, low cost, high electrocatalytic activity, and multiple valence states. The catalytic activity of manganese oxides depends on their chemical composition, structure, morphology, and preparation method. For example, the order of ORR catalytic activity for phases of manganese oxide is as follows: $\gamma\text{-MnOOH} > \text{Mn}_2\text{O}_3 > \text{Mn}_3\text{O}_4 > \text{Mn}_5\text{O}_8$.¹² The catalytic activities for MnO_2 of different phases are demonstrated as $\alpha\text{-MnO}_2 \approx \delta\text{-MnO}_2 > \gamma\text{-MnO}_2 > \lambda\text{-MnO}_2 > \beta\text{-MnO}_2$.¹³ Similar to

manganese dioxide, hydroxyl manganese oxide (MnOOH) also shows good catalytic activity toward ORR.¹⁴ Ohsaka et al.^{15, 16} compared the ORR on a MnOOH-modified electrode and a superoxide dismutase (SOD) modified electrode and found that the MnOOH possesses excellent catalytic activity not only for the disproportionation of the produced $O_2^{\cdot-}$ into O_2 and HO_2^- , but also for that of the produced HO_2^- into O_2 and OH^- . In addition, a significant enhancement of the electrocatalytic activity toward the ORR in alkaline media was observed when γ -MnOOH nanorod was electrodeposited onto Pt electrode.¹⁷ MnOOH or MnO_2 is often mixed with carbon materials for the ORR activity characterizations,^{3, 16, 18} which due to their low electrical conductivity. Carbon materials not only can increase the electronic conductivity of the electrode, but also have relatively good ORR catalytic activity in the alkaline media.¹⁹ Among them, three-dimensional (3D) graphene structural materials have been considered as alternative catalyst support to improve catalytic performance, owing to their unique network structure, large specific surface area, being light-weight, enhanced electron and ion transport, good mechanical integrity and outstanding electrical properties.^{20, 21} Recently, researchers have tried to fabricate the framework of manganese oxides supported on graphene aerogel by chemical methods. For instance, Wang et al.²² reported that MnO_2 /nanoporous 3D graphene prepared by a mild hydrothermal method showed good performance as supercapacitor electrode material. Zhu and co-workers²³ synthesized the graphene/ α - MnO_2 3D network by a facile hydrothermal method showed high performance as anode for lithium ion battery. Yan et al.²⁴ demonstrated that 3D graphene/ MnO_2 hybrid

exhibited superior catalytic and cycle performance as the cathode material in a Li–O₂ battery. Nevertheless, most work about manganese oxides supported on graphene aerogel is applied for lithium ion batteries and supercapacitors, the reports of using this hybrid material as ORR catalysts are still limited.

Graphene quantum dots (GQDs), zero-dimensional carbon nanostructures with a size below 10 nm and a single atomic layer of nano-sized graphite, which display unusual chemical and physical properties due to their strong quantum confinement and edge effects.^{25, 26} Hence, GQDs have been applied in many fields, such as biological science,²⁷ photocatalysis,²⁸ light-emitting,^{29, 30} sensors,^{31, 32} and so on. However, the development and application of GQDs remain inchoate, especially in the case of electrocatalysis. The surface of GQDs has many oxygen-rich functional groups. Thus, the electroneutrality of GQDs is broken, generating a large number of positively charged active sites for the O₂ surface adsorption. Moreover, the active sites on the edge of GQDs are also very advantageous in promoting ORR. Recently, Valentin et al.³³ reported multiple doped graphene quantum dots favored a four-electron reduction of oxygen to water. Qu et al.²⁶ proposed that N-doped GQDs with the feature of oxygen-rich functional groups exhibited superior electrocatalytic ability for ORR. In addition, Li et al.³⁴ also demonstrated that nitrogen-functionalised GQDs showed a highly size-dependent electrocatalytic activity. Moreover, due to their small dimension, GQDs can be easily interfaced to other nanomaterials in order to build more complex systems. For example, Chen et al.³⁵ demonstrated that graphene quantum dots-supported Pt nanoparticles showed drastic enhancement ORR

catalytic activity, in comparison to commercial Pt/C catalysts. Qu et al.³⁶ proposed that a novel metal-free catalyst composed of GQDs and multi-walled carbon nanotubes (MWCNTs) exhibited a significant synergistic effect on enhanced catalytic activity for ORR.

In this paper, we demonstrated a facile approach to synthesize the three-dimensional (3D) graphene aerogel supported and zero-dimensional GQDs-modified one-dimensional (1D) γ -MnOOH nanotubes as a highly active electrocatalyst. The hybrid exhibits a higher catalytic activity for the ORR in alkaline media than that of γ -MnOOH@GA, γ -MnOOH nanotubes, and GA. Such particular conformation not only provides a large amount of active sites for ORR, but also is beneficial for the fast transport of oxygen and charges. To the best of our knowledge, this is the first time to fabricate γ -MnOOH@GA/GQDs hybrid as an efficient catalyst for ORR.

2. Experimental

2.1 Preparation of graphene aerogel

Graphene oxide (GO) was synthesized from natural graphite by modified Hummer's method.³⁷ Graphene aerogel was prepared by chemical reduction and self-assembly of GO sheets using ethylene glycol as the reducing agent. In a typical synthesis, 40 mg of GO was dispersed in 40 mL of deionized (DI) water and sonicated for at least 0.5 h to form a homogeneous suspension with the concentration of 1 mg mL⁻¹. 10 mL of ethylene glycol solution was slowly added into the suspension and mixed using a magnetic stirrer for 0.5 h. Subsequently, the mixed suspension was

transferred into a Teflon-lined autoclave and heated at 180 °C for 12 h. Then, the products were centrifuged several times with DI water and ethanol to remove any impurities and freeze-dried for one day to remove absorbed water to obtain graphene aerogel (GA). The as-prepared GA was placed in the center of the furnace tube and heated from room temperature to 450 °C in Ar atmosphere. The heating rate was 10 °C min⁻¹ and heating time was 1 h.

2.2 Preparation of graphene quantum dots

The graphene quantum dots (GQDs) were prepared by using a simple electrochemical (EC) procedure.³⁸ The EC preparation of GQDs was carried out at 25 °C in a standard three-electrode cell, using a platinum foil as the counter electrode, a saturated Ag/AgCl/Cl⁻ electrode as the reference electrode, and a piece of reduced graphene oxide (rGO) film (5 mm × 10 mm) as working electrode, cycling the potential between ± 3.000 V (*vs.* Ag/AgCl) at a scan rate of 500 mV s⁻¹. The reduced graphene oxide was prepared with aqueous N₂H₄ in the presence of ammonia. Briefly, 50 mL of 0.5 mg mL⁻¹ graphene oxide dispersion was treated with 350 μL of concentrated ammonium hydroxide and 50 μL of hydrazine monohydrate (35%) for 1 h at 90 °C. The freestanding reduced graphene oxide film was made by direct filtration of the aqueous reduced graphene oxide colloidal suspension through a filter membrane with a pore size of 0.22 μm. The electrolyte was 0.1 M phosphate buffer solution (PBS). The rGO film was fixed with a clamp of electrochemical workstation and contact with the electrolyte. The pure water-soluble GQDs were collected after 500 potential cycles.

2.3 Preparation of the GA-supported, and GQDs-modified γMnOOH nanotubes

hybrid

The $\gamma\text{MnOOH}@GA$ hybrid was prepared by hydrothermal treatment. 0.3 mmol of $\text{MnSO}_4\cdot\text{H}_2\text{O}$ and 0.9 mmol of KMnO_4 were added to 50 mL of 4:1 (v/v) water/ethylene glycol mixed solvent and stirred for 30 min. The solution was then transferred into a 100 mL Teflon-lined autoclave. A big piece of the as-prepared graphene aerogel was immersed into the autoclave, which was sealed and heated at 180 °C for 14 h. The autoclave was naturally cooled to room temperature, then the precipitate was collected and centrifuged several times with DI water and ethanol to remove any impurities and excessive metal ions. The obtained black precipitation dried at 60 °C in a vacuum oven for overnight. The product was calcinated at 450 °C for 1 h to get $\gamma\text{MnOOH}@GA$ hybrid. Then, 50 mg of $\gamma\text{MnOOH}@GA$ was added into 5 mL GQDs solution under magnetic stirring vigorously for 2 h. Finally, the mixture was dried at 65 °C in a vacuum oven for 10 h to obtain $\gamma\text{MnOOH}@GA/GQDs$ hybrid.

2.4 Materials characterization

X-ray diffraction (XRD, D/Max2250, Rigaku Corporation, Japan) analysis was performed to determine the crystal structure of the samples using nickel-filtered $\text{Cu K}\alpha$ radiation ($\lambda = 1.5406 \text{ \AA}$), the diffraction angle ranging from 10° to 80° with a rate of 1.0° min^{-1} . UV–vis spectra of GQDs solution was carried out on a TU-1901 (Puxi Current Technologies, Beijing) spectrometer with a 0.5 cm quartz cell and a bandwidth setting of 2 nm at a scan speed of 1200 nm min^{-1} . The morphology and energy dispersive X-ray (EDX) spectra were investigated by a field emission scanning electron microscope (FESEM, Nova NanoSEM 230). The microstructure was

measured by a high resolution transmission electron microscope (HRTEM, FEI TECNAI G2 F20) operated at 120 kV. Raman spectra was measured by a LabRAM Hr800 confocal Raman microscopic system with a 532 nm excitation laser. The surface elemental analysis of $\gamma\text{MnOOH@GA/GQDs}$ was performed by X-ray photoelectron spectroscopy (XPS, K-Alpha 1063, Thermo Fisher Scientific) spectrometer using monochromatized Al Ka (1486 eV) radiation. The measurement parameters were as follows: 20 eV pass energy, 0.1 eV energy increments.

2.5 Cyclic voltammetry and impedance spectroscopy measurements

The measurements were carried out via an electrochemical analyzer (Zennium, Zahner, Germany) in a standard three-electrode cell at room temperature. A three-electrode cell configuration was consisted of a working electrode with glassy carbon electrode of 3 mm in diameter, a counter electrode with platinum foil and a reference electrode with Ag/AgCl in 3 M KCl. The electrolyte was 0.1 M KOH aqueous solution. The catalyst ink was prepared by mixing 4 mg of catalytic material and 13 μL 5 wt.% Nafion solution dispersed in 1 mL of 1:4 (v/v) water/isopropanol mixed solvent, then ultrasonicated for at least 40 min to form a homogeneous suspension. 5 μL of the prepared catalytic ink was dropped onto a glassy carbon electrode and dried in air, resulting in the loading of around 0.25 mg cm^{-2} for all the catalysts. The electrolyte was deaerated by purging high-purity O_2 for at least 30 min before each electrochemical measurement and a flow of O_2 was maintained over the electrolyte during electrochemical measurements. In compared experiments, CV measurements were performed in N_2 (99.99% pure) saturated electrolyte. Cyclic

voltammograms were conducted from -1.2 to 0.2 V (*vs.* Ag/AgCl) at a scan rate of 50 mV s⁻¹. The EIS measurement was performed with the alternative current (AC) voltage amplitude of 5 mV, the voltage frequency ranging from 100 KHz to 0.01 Hz and the applied potential of -0.2 V (*vs.* Ag/AgCl).

2.6 Rotating disk electrode measurements

The measurements were also carried out by a three-electrode cell configuration. The working electrode is glassy carbon rotating disk electrode (RDE) of 5.0 mm in diameter (Pine Instrument Company, USA). The catalyst ink was prepared by mixing 4 mg of catalytic material and 15 μ L of 5 wt.% Nafion (D-521, Alfar Aesar) solution dispersed in 300 μ L isopropanol, then ultrasonicated for about 40 min to form a homogeneous suspension. 5 μ L of the prepared catalytic ink was dropped onto a glassy carbon RDE and dried in air, giving the loading of around 0.25 mg cm⁻² used for all the catalysts. The linear sweep voltammograms (LSV) was recorded from -1.0 to 0.2 V (*vs.* Ag/AgCl) at a scan rate of 5 mV s⁻¹ with various rotation rates (400 , 625 , 900 , 1225 , and 1600 rpm).

3. Results and discussions

3.1 Characterizations of catalytic materials

The high resolution TEM (HRTEM) images (Figure S1, in supporting information) reveal that GQDs have the diameters of $2 \sim 10$ nm with an average value of ~ 4 nm and obvious lattice fringe, which further confirm the good crystalline nature. GQDs show good dispersion without obvious aggregation. The UV-vis absorption spectrum of the dispersed yellow GQDs illuminated under UV light (365 nm) shows

an absorption band at ca. 360 nm (Figure S2), which may be assignable to the $n-\pi^*$ transition of the functional group containing oxygen.^{39,40}

This work introduces a facile approach to prepare novel $\gamma\text{MnOOH@GA/GQDs}$ nanohybrid material, as shown in Fig. 1. Briefly, the reduction of GO at 180 °C for 12 h leads to strong $\pi-\pi$ interactions between the reduced graphene oxide (rGO) layers, facilitating self-assembly into the GA monolith. The electrochemically assisted formation of GQDs involves the oxidation of the C-C bonds and the interaction of the electrolyte ions into the structure of rGO electrode, with the consequent release in solution of GQDs³³. $\gamma\text{MnOOH@GA}$ was synthesized by hydrothermal treated at 180 °C using prepared GA and metal ions.

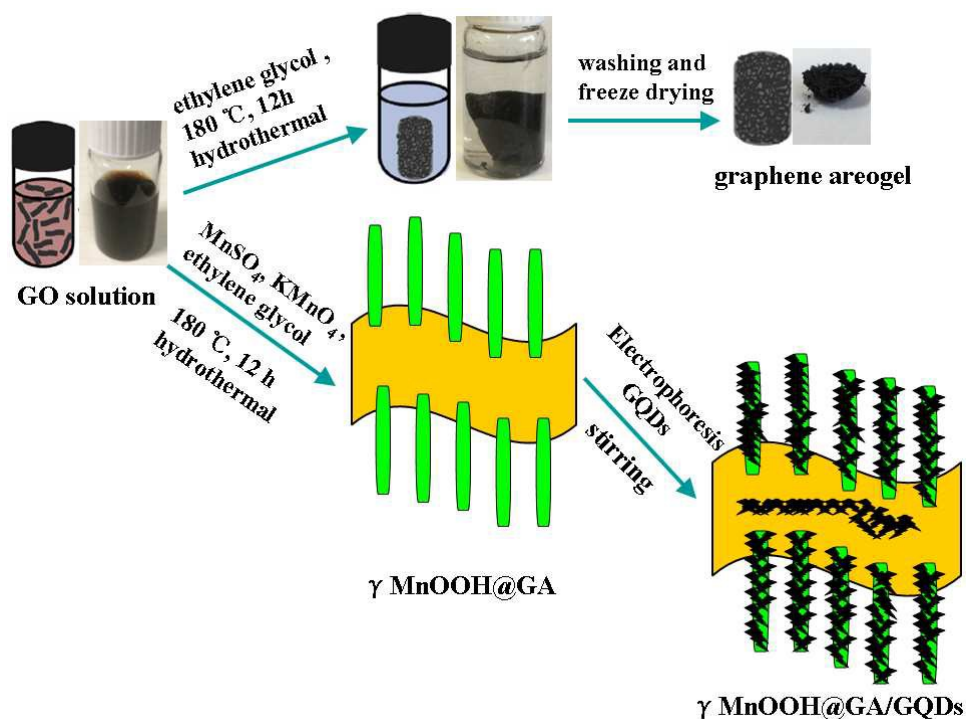


Figure 1. Schematic illustration for the synthesis of graphene aerogel and $\gamma\text{MnOOH@GA/GQDs}$ hybrid.

The X-ray diffraction (XRD) patterns of graphene aerogel, $\gamma\text{MnOOH@GA}$, and

γ MnOOH@GA/GQDs were shown in Fig. 2. The characteristic diffraction peaks of γ MnOOH@GA/GQDs hybrid are at $2\theta = 18.35^\circ, 26.15^\circ, 33.94^\circ, 37.22^\circ, 39.65^\circ, 41.07^\circ, 51.75^\circ, 54.86^\circ, 54.94^\circ, 55.55^\circ, 61.80^\circ, 71.15^\circ$, which correspond to the (100), (11-1), (020), (200), (12-1), (012), (022), (22-2), (31-1), (13-1), (131), and (20-4) planes of cubic γ MnOOH structure (JCPDS card No. 41-1379) with a space group $P21/c(14)$ without any impurity. No graphene aerogel peak at 22.94° (002) is observed, which indicates that γ MnOOH nanotubes were efficiently deposited on the GA surface. The lattice constants are calculated from the diffraction profile and $a = 5.30$, $b = 5.28$ and $c = 5.31$ Å, which are in agreement with the value of γ MnOOH from JCPDS file. After adding GQDs, the diffraction peaks of γ MnOOH can be well indexed, indicating that the GQDs have negligible influence on the intrinsic crystallinity of γ MnOOH.

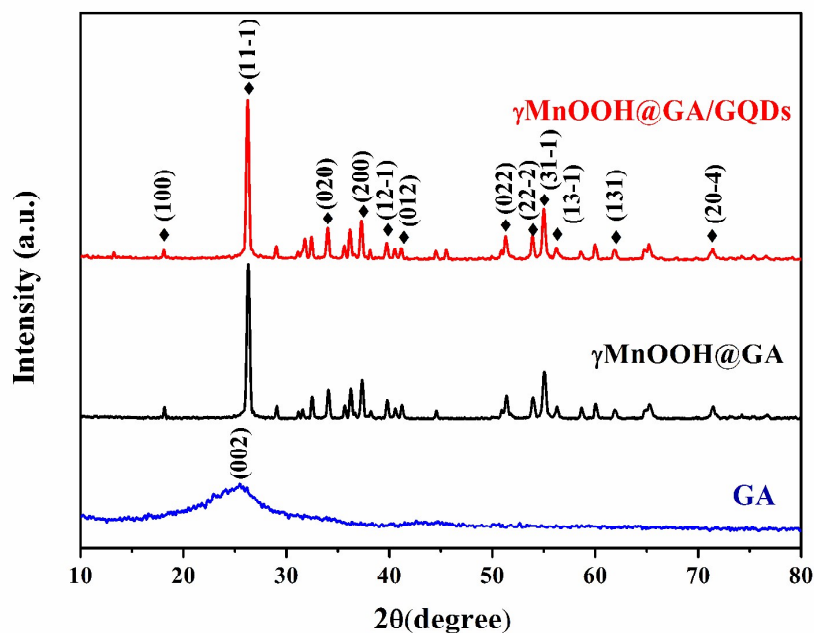


Figure 2. X-ray diffraction (XRD) spectrum of GA, γ MnOOH@GA hybrid and γ MnOOH@GA/GQDs hybrid, respectively.

The morphology and structure of $\gamma\text{MnOOH}@GA/GQDs$ hybrid were investigated by scanning electron microscope (SEM) and transmission electron microscope (TEM). The SEM images of $\gamma\text{MnOOH}@GA/GQDs$ hybrid (Fig. 3) clearly exhibit that γMnOOH nanotubes with the diameters of about 100 nm anchor uniformly on the porous graphene aerogel sheets, suggesting efficient assembly between the γMnOOH nanotubes and GA sheets during the solvothermal treatment. As shown in Fig. 4a, γMnOOH nanotubes anchor on the chiffon shape graphene aerogel sheets. The HRTEM images (Fig. 4b,c) show that the γMnOOH nanotubes have obvious lattice fringe with spacing of 0.30 nm, corresponding to the (31-1) lattice planes, and GQDs dispersed on the γMnOOH nanotubes with lattice spacing of 0.22 nm. The SEM images of GA and $\gamma\text{MnOOH}@GA$ were shown in Fig. S3 and the TEM image of GA/GQDs was shown in Fig. S4, the GQDs, γMnOOH tubes, and graphene aerogel can be identified clearly. Energy dispersive X-ray spectrometry (EDS) analysis of $\gamma\text{MnOOH}@GA/GQDs$ confirms the existence of C (56.47 At%), O (29.64 At%), Mn (12.16 At%), and K (1.73 At%) elements. The K to Mn ratio correlates the information with the oxidation states of manganese, which has been highlighted as a key in the oxygen reduction reaction.⁴¹ The $\gamma\text{MnOOH}@GA$ hybrid was synthesized using KMnO_4 , K^+ ions served as intercalated cations of the γMnOOH nanotubes. The lower concentration of K^+ makes the Mn^{4+} content decrease, leading to a high ratio of $\text{Mn}^{3+}/\text{Mn}^{4+}$. The EDS spectrum of $\gamma\text{MnOOH}@GA$ hybrid was shown in Fig. S5. The $\gamma\text{MnOOH}@GA/GQDs$ hybrid presents the higher K/Mn atomic

ratio (0.142) than that of $\gamma\text{MnOOH@GA}$ hybrid (0.025), leading to a high ratio of $\text{Mn}^{3+}/\text{Mn}^{4+}$, whereas the Mn^{3+} reduced ions are suggested to be the active sites in recent studies for oxygen reduction.^{12, 42, 43} So $\gamma\text{MnOOH@GA/GQDs}$ hybrid possesses more active sites.

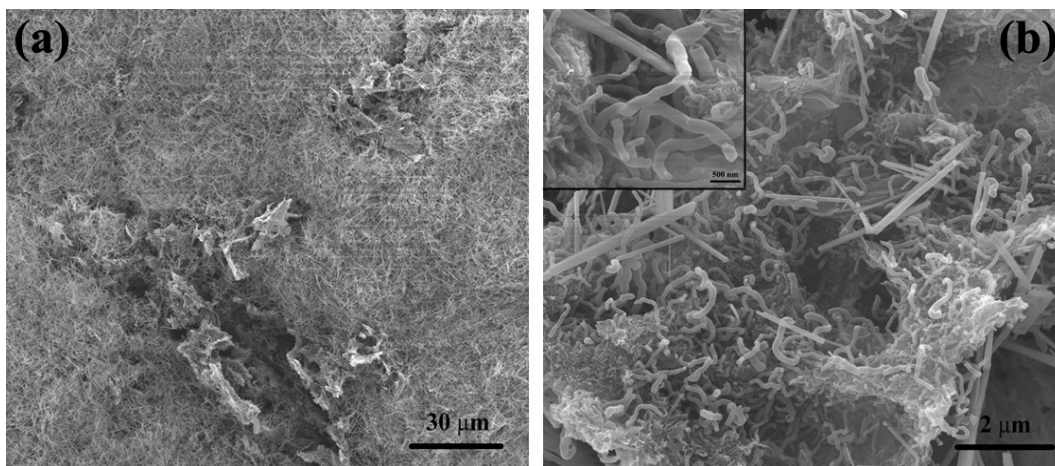


Figure 3. SEM images of $\gamma\text{MnOOH@GA/GQDs}$ hybrid at different magnification.

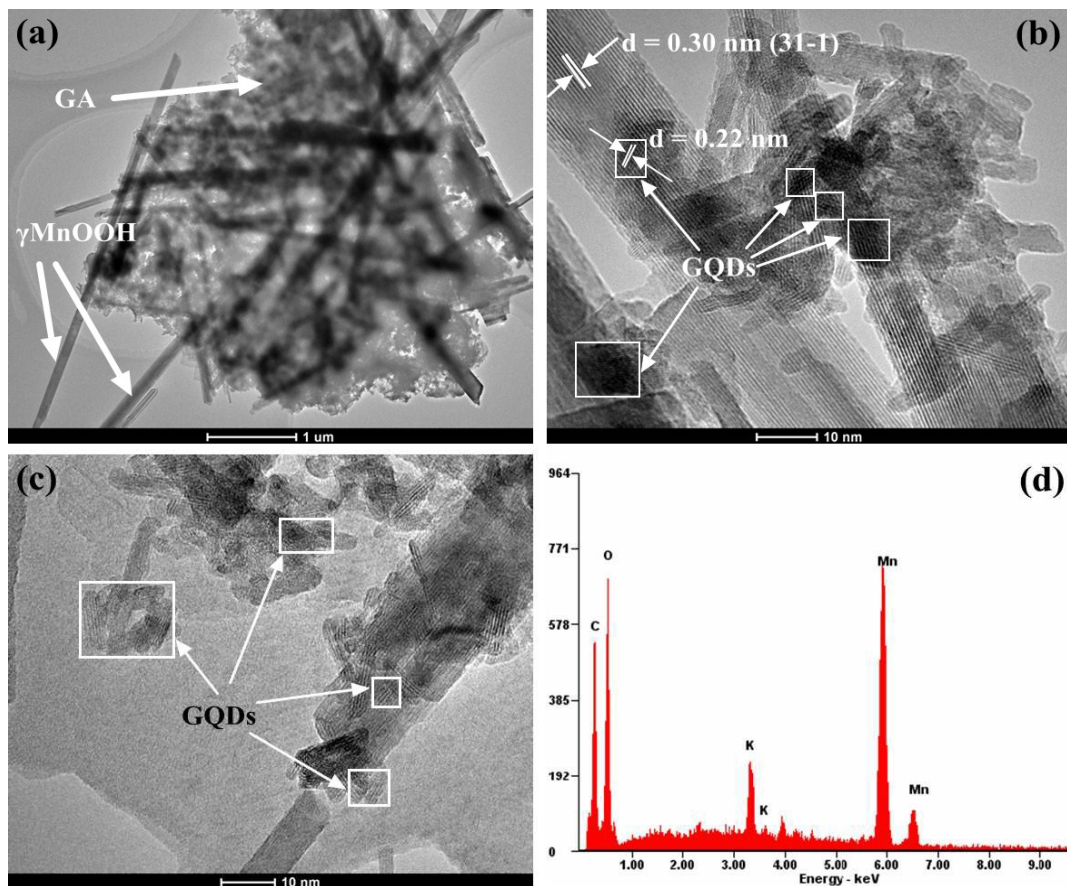


Figure 4. TEM images of (a) $\gamma\text{MnOOH@GA/GQDs}$; HRTEM image of (b, c) $\gamma\text{MnOOH@GA/GQDs}$; EDS spectrum of (d) $\gamma\text{MnOOH@GA/GQDs}$.

Raman spectroscopy is a very powerful tool to characterize carbon materials. In this work, it was used to investigate the structure of $\gamma\text{MnOOH@GA/GQDs}$ hybrid and the interaction between γMnOOH nanotubes and GA sheets. Raman spectra of $\gamma\text{MnOOH/GQDs}$, $\gamma\text{MnOOH@GA}$ and $\gamma\text{MnOOH@GA/GQDs}$ is listed in Fig. 5a. The D band at 1350 cm^{-1} and the G band at 1580 cm^{-1} reveal the presence of graphene aerogel. The D band is attributed to the breathing mode of sp^2 -rings and requires a defect for its activation by an intervalley double-resonance (DR) Raman process.⁴⁴ The G band corresponds to the doubly degenerate E_{2g} phonons at the Brillouin zone center.⁴⁵ Thus, the D to G band peak intensity ratio, I_D/I_G , is generally used to verify

the degree of defects of the carbon nanomaterials. The I_D/I_G of $\gamma\text{MnOOH@GA/GQDs}$ is 0.936, which is relatively higher than that of $\gamma\text{MnOOH@GA}$ (0.910), implying that the size of the sp^2 domains and defects increased during the modification of GQDs. Furthermore, the broad D band and G band with weak intensity of $\gamma\text{MnOOH@GA/GQDs}$ would be due to the interaction between γMnOOH nanotubes and GA sheets.^{46,47} New prominent peak at about 640 cm^{-1} appears in the spectrum of all the materials, which is usually attributed to the (Mn–O) stretching vibration in the basal plane of MnO_6 sheet.^{48,49}

X-ray photoelectron spectroscopy (XPS) can be employed to investigate the surface elemental compositions and electronic configurations of the catalysts. As shown in the survey scan of $\gamma\text{MnOOH@GA/GQDs}$ (Fig. 5b), carbon (44.79 At%), and oxygen (43.66 At%), manganese (11.2 At%), and potassium (0.35 At%) can be detected. Notably, the surface Mn/O atomic ratio of $\gamma\text{MnOOH@GA/GQDs}$ is much lower than the stoichiometric ratio of γMnOOH (Mn/O = 1/2), signifying some oxygen-containing functional groups (hydroxyl and carboxyl) still locate on the edges of graphene aerogel and GQDs. It can be seen from Fig. 5c that the Mn2p spectrum exhibits two peaks at 641.69 and 653.79 eV can be referred to the binding energies of the $2p_{3/2}$ and $2p_{1/2}$, respectively. The energy separation between the two peaks is 12.1 eV, which is in agreement with the literature on mixed valence of Mn element.^{50,51} The main peaks and satellite peaks indicate the presence of Mn(III) and Mn(IV) cations. In the Mn3s spectra, two peaks at 83.29 and 89.19 eV with the splitting value of 5.9 eV were observed (Fig. 5d), which can be ascribed to the mixed valence state

of Mn(III) and Mn(IV).^{42, 52} As shown in Fig. 5e, the C1s spectra of γ MnOOH@GA/GQDs can be assigned to the following carbon components: C–C (sp^2), C–O and C=O groups, respectively.^{53, 54} Contrary to the high-intensity peak for C–C (284.7 eV) and the broad peak for C–O (285.6 eV) groups, the intensity for C=O groups is weak, which illustrates that GO is reduced into GA with most of oxygen atoms removed. As shown in Fig. 5f, the O1s spectra can be divided into the peaks at 531.74 and 530.69 eV, corresponding to the binding energy of C=O, OH functionalities.

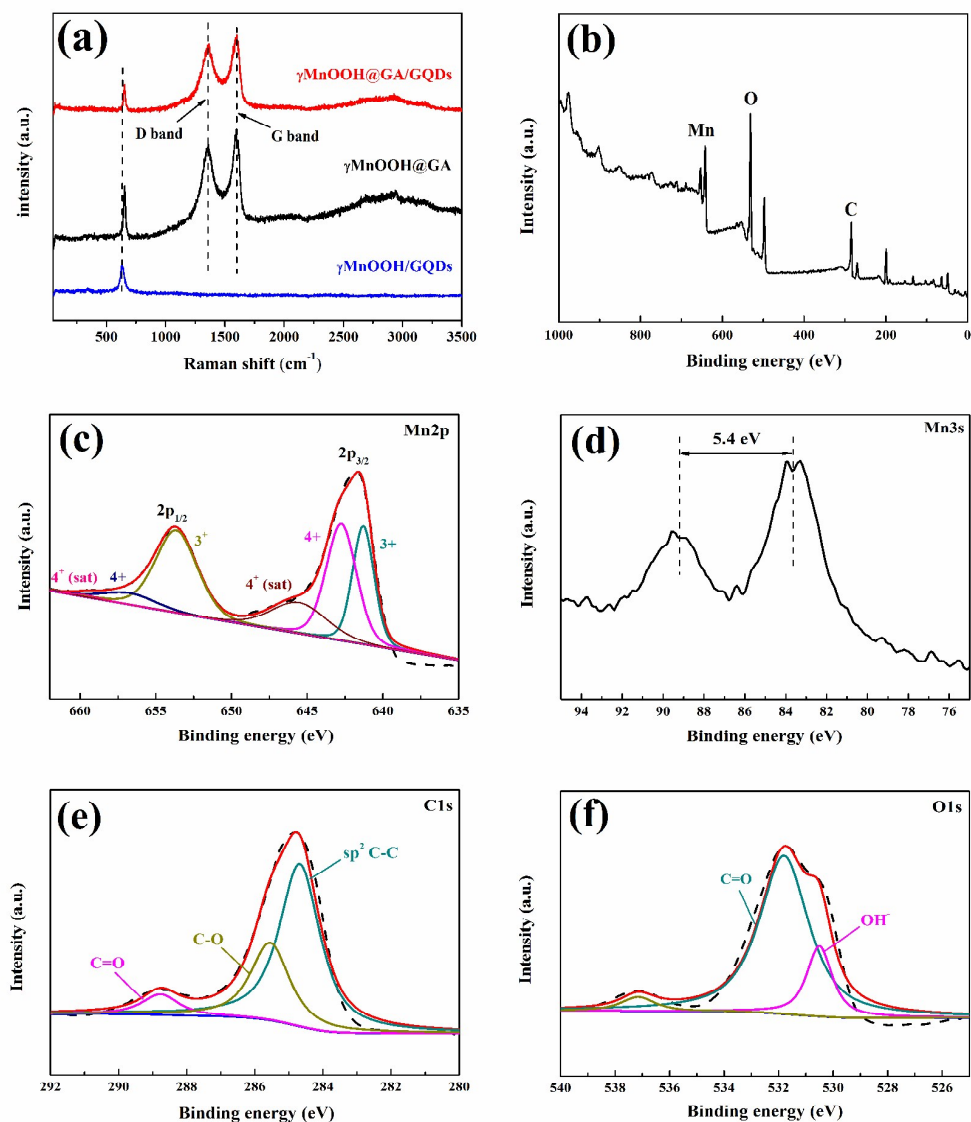


Figure 5. (a) Raman spectra of $\gamma\text{MnOOH}/\text{GQDs}$, $\gamma\text{MnOOH}@/\text{GA}$, and $\gamma\text{MnOOH}@/\text{GA}/\text{GQDs}$, respectively. The laser excitation wavelength is 532 nm. (b) XPS spectra of $\gamma\text{MnOOH}@/\text{GA}/\text{GQDs}$ hybrid; High-resolution XPS spectra of $\gamma\text{MnOOH}@/\text{GA}/\text{GQDs}$: (c) Mn2p, (d) Mn3s, (e) C1s, and (f) O1s, respectively.

3.2 Electrocatalytic activity of the nanohybrid for oxygen reduction reaction

The ORR catalytic activity of $\gamma\text{MnOOH}@/\text{GA}/\text{GQDs}$ hybrid was investigated by cyclic voltammograms (CV) in N_2 and O_2 saturated 1.0 M KOH at a scan rate of 50

mV s⁻¹, respectively. The current densities of the catalysts were calculated using the electrode geometric area. As shown in Fig. 6, cyclic voltammograms without any peaks are obtained in the presence of N₂ for all catalysts. In contrast, apparent reduction peaks at about -0.20 ~ -0.50 V (*vs.* Ag/AgCl) are observed when O₂ is introduced. The peak potential of γ MnOOH@GA/GQDs hybrid (-0.28 V *vs.* Ag/AgCl) is 10 mV more positive than that of γ MnOOH@GA (-0.29 V *vs.* Ag/AgCl), which is even more positive than that of GA (-0.31 V *vs.* Ag/AgCl), γ MnOOH/GQDs hybrid (-0.42 V *vs.* Ag/AgCl), and γ MnOOH nanotubes (-0.43 V *vs.* Ag/AgCl). The reduction peak at about -0.40 V (*vs.* Ag/AgCl) was corresponded to the reduction process of O₂ to HO₂⁻.⁵⁵ The addition of GA and GQDs brings the peak potential more positive, so γ MnOOH@GA/GQDs hybrid can promote this process. These results indicate that γ MnOOH@GA/GQDs hybrid obtain better ORR catalytic activity for ORR, which may be due to the synergistic effect between the γ MnOOH nanotubes and graphene aerogel and the effect of GQDs.

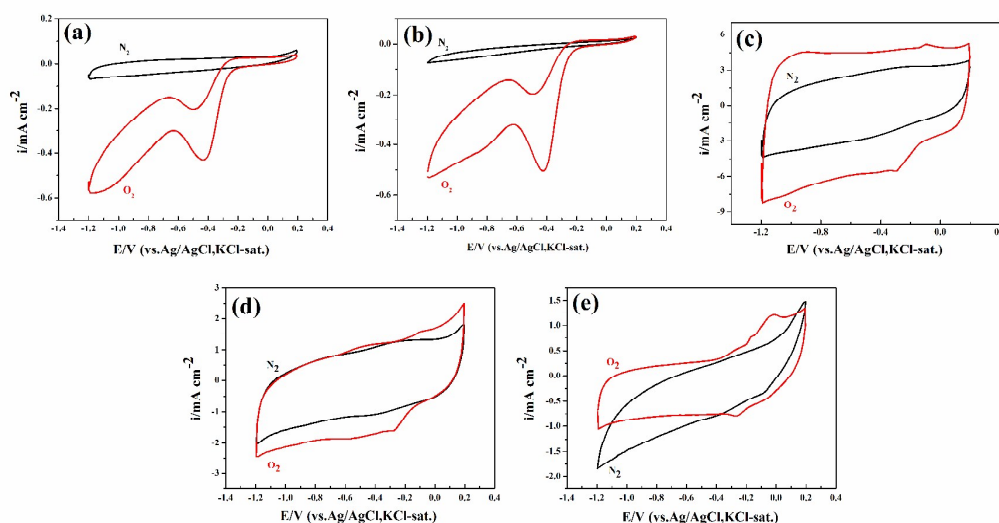


Figure 6. Cyclic voltammograms obtained for (a) γ MnOOH, (b) γ MnOOH/GQDs, (c)

GA, (d) $\gamma\text{MnOOH@GA}$, (e) $\gamma\text{MnOOH@GA/GQDs}$ electrocatalysts in O_2 -saturated and N_2 -saturated 0.1 M KOH aqueous solution.

RDE measurements were further employed to investigate the ORR kinetics of the $\gamma\text{MnOOH@GA/GQDs}$ hybrid material. For comparison, the linear sweep voltammetry (LSV) curves of $\gamma\text{MnOOH@GA}$, $\gamma\text{MnOOH/GQDs}$, GA, γMnOOH , and commercial 20 wt.% Pt/C catalysts at a scan rate of 10 mV s^{-1} with a rotation rate of 1600 rpm were shown in Fig. 7a. The $\gamma\text{MnOOH@GA/GQDs}$ hybrid shows the onset potential for the oxygen reduction at 0.13 V, which is more positive than that of $\gamma\text{MnOOH@GA}$, $\gamma\text{MnOOH/GQDs}$, GA, and γMnOOH , and is comparable with that of 20 wt.% Pt/C. In the mixed kinetic- and diffusion-limiting region ($-0.35 \sim 0 \text{ V}$), the mass transport plays an important role. The ORR activity can be evaluated by the half-wave potentials, $E_{1/2}$ (the potential at which the current reaches half its diffusion-limited value). The half-wave potentials of all the catalyst follow the same trend as that of onset potentials, indicating the fast reaction kinetics of $\gamma\text{MnOOH@GA/GQDs}$ in catalyzing ORR. Wide current plateaus in the LSV curves of $\gamma\text{MnOOH@GA/GQDs}$ and $\gamma\text{MnOOH@GA}$ are considered to be diffusion-controlled processes, corresponding to efficient four-electron-dominated ORR pathways, which is the same as the case of Pt/C catalyst. The Tafel slopes calculated from the E versus $\log(J_k)$ curves in O_2 -saturated 0.1 M KOH aqueous solution were shown in Fig. 7c. The smaller Tafel slope indicates the higher intrinsic catalytic activity for ORR. The $\gamma\text{MnOOH@GA/GQDs}$ hybrid exhibits a Tafel slope of 82.7 mV dec^{-1} at low overpotentials, which is close to that of the 20 wt.% Pt/C

catalyst and smaller than that of the $\gamma\text{MnOOH@GA}$, GA, and γMnOOH catalysts. It is indicated that $\gamma\text{MnOOH@GA/GQDs}$ hybrid has a faster reaction kinetic, and GQDs can further improve the catalytic activity, resulting in lower overpotential. The electrocatalytic kinetic properties including the onset potential, half-wave potential and Tafel slopes are summarized in Table 1. The electrocatalytic kinetics of $\gamma\text{MnOOH@GA/GQDs}$ hybrid is superior to those of other four catalysts, confirming the importance of the synergistic effect and GQDs modifying. In addition, the comparison of MnOOH@GA/GQDs , $\gamma\text{MnOOH@GA}$, $\text{MnOOH@carbon black}$ and $\text{MnOOH@carbon black/GQDs}$ was conducted to further discuss the catalytic activity of the hybrid materials. As shown in Fig. S6, the $\gamma\text{MnOOH@GA}$ and MnOOH@GA/GQDs hybrids has better catalytic activity than the $\text{MnOOH@carbon black/GQDs}$ and $\text{MnOOH@carbon black}$ hybrids, respectively. These results highlight the improved ORR activity of $\gamma\text{MnOOH@GA/GQDs}$, which demonstrates that the 3D architecture structural GA helps to enhance the charge transfer and the electrical conductivity of γMnOOH , and GQDs actually facilitate ORR electrocatalytic activity. The superior electrocatalytic performance of our nanohybrid material is remarkable in comparison to other similar metal-free composite catalysts in alkaline solution.⁵⁶⁻⁵⁸

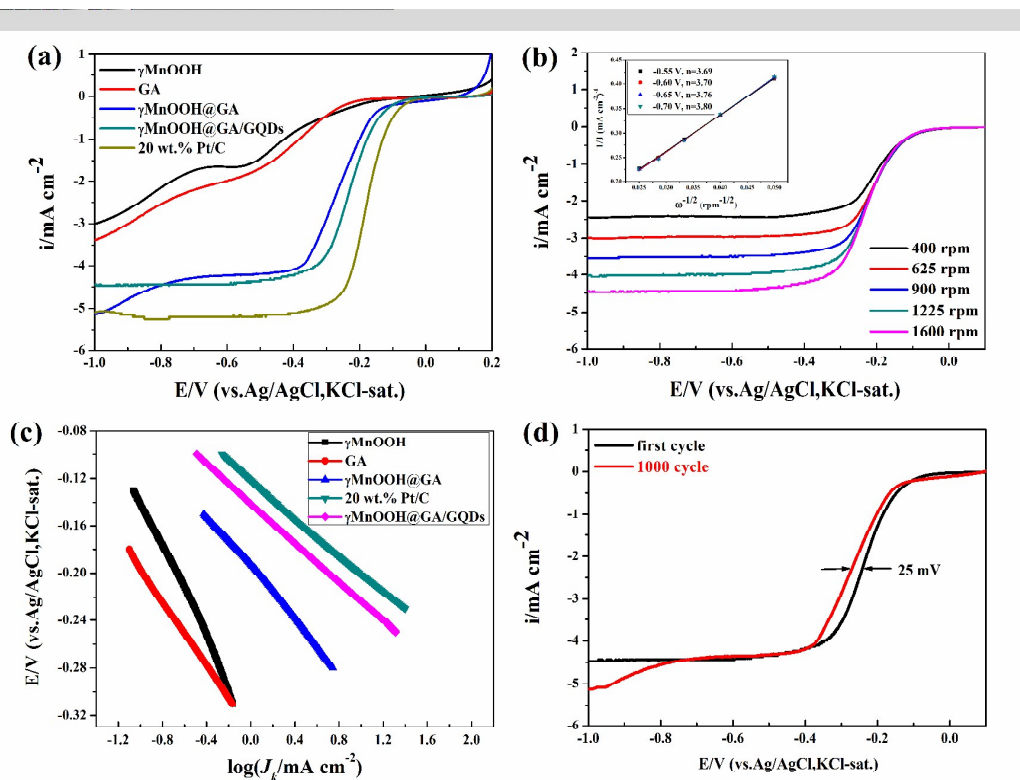


Figure 7. (a) LSV curves of γ MnOOH, GA, γ MnOOH@GA, γ MnOOH@GA/GQDs, and 20 wt.% Pt/C catalysts on RDE electrode in O₂-saturated 0.1 M KOH solution at a rotation rate of 1600 rpm with a scan rate of 5 mV s⁻¹; (b) LSV curves of γ MnOOH@GA/GQDs hybrid in O₂-saturated 0.1 M KOH solution at various rotation rates with a scan rate of 5 mV s⁻¹, the inset shows the corresponding Koutecky–Levich plots at different potentials; (c) Tafel slopes from RDE cures; (d) Durability of γ MnOOH@GA/GQDs hybrid. The durability test was performed in O₂-saturated 0.1 M KOH electrolyte before and after 1000 extensive cycles.

Table 1. ORR kinetic parameters for the various catalysts investigated in this study.

catalyst	onset potential (V vs Ag/AgCl)	half-wave potential (V vs Ag/AgCl)	Tafel slope (mV dec ⁻¹)
γ MnOOH	-0.03	-0.40	194.9
GA	0.08	-0.39	135.3
γ MnOOH@GA	0.09	-0.26	110.9
γ MnOOH@GA/GQDs	0.11	-0.23	82.7
20% Pt/C	0.13	-0.17	78.5

To gain further insights into the ORR mechanism of γ MnOOH@GA/GQDs, the RDE measurements at different rotation rates (400, 625, 900, 1225, and 1600 rpm) in O₂-saturated 0.1 M KOH solution with a scan rate of 5 mV s⁻¹ were employed. The polarization curves and the corresponding Koutecky-Levich (K-L) plots at the potential range from -0.70 to -0.55 V are shown in Figure 7b. The corresponding RDE results at different rotation rates of γ MnOOH@GA were illustrated in Fig. S7 as compared. The electron transfer number (*n*) in the ORR is calculated by Koutecky-Levich (K-L) equation as below:⁵⁹

$$\frac{1}{J} = \frac{1}{J_k} + \frac{1}{J_L} = \frac{1}{J_k} + \frac{1}{B\omega^{1/2}} \quad (1)$$

$$B = 0.2nFD_o^{2/3} \nu^{-1/6} C_o \quad (2)$$

$$J_k = nFkC_o \quad (3)$$

where *J* is the measured current density, *J_k* is the kinetic current density, and *J_L* is the diffusion-limiting current density. ω is the angular velocity (rpm), *n* is the transferred

electron number, F is the Faraday constant (96500 C mol^{-1}), D_o is the diffusion coefficient of O_2 in 0.1 M KOH ($1.9 \times 10^{-5} \text{ cm}^2 \text{ s}^{-1}$), C_o is the bulk concentration of O_2 ($1.2 \times 10^{-6} \text{ mol cm}^{-3}$), ν is the viscosity of the electrolyte ($1.0 \times 10^{-2} \text{ cm}^2 \text{ s}^{-1}$), and k is the electron transfer rate constant.⁴² The calculated electron transfer numbers for $\gamma\text{MnOOH@GA/GQDs}$ at different potential are 3.60 (-0.55 V), 3.70 (-0.60 V), 3.76 (-0.65 V), and 3.80 (-0.70 V), respectively, close to 4, suggesting that the composite material favors a higher selectivity for the four-electron pathway toward ORR. The morphology of $\gamma\text{MnOOH@GA/GQDs}$ catalyst after oxygen reduction reaction was also tested, as shown in Fig. S8. The hybrid material retained coupling between the nanotubes and graphene aerogel without any detachment after the RDE measurements at different rotation rates. Further, the porous nature of hybrid material was retained. There was no obvious change and breakdown of $\gamma\text{MnOOH@GA/GQDs}$ hybrid after oxygen reduction reaction, which demonstrated the material had high structural stability.

Durability of the electrocatalysts is another important parameter in judging their practical applications. To this end, cycling durability test in O_2 -saturated 0.1 M KOH electrolyte was carried out to evaluate the stability of $\gamma\text{MnOOH@GA/GQDs}$ before and after 1000 cycles between -1.0 and 0.2 V at 1600 rpm rotation rate. As shown in Figure 7d, after 1000 potential sweeps, the polarization curve only shows 35 mV positive shift in onset potential, no significant change in the limiting current, and only 25 mV negative shift in the half-wave potential, indicating the high durability of the hybrid catalyst.

The electrochemical impedance spectroscopy (EIS) can be used to investigate the interfacial processes and kinetics of electrode reactions in electrochemical systems. The Nyquist plots reflect the relationship of the imaginary impedance $-Z''$ versus the real impedance Z' , and the corresponding equivalent-circuit model is displayed in Figure 8. The Nyquist plots mainly consist of arc-like profiles for all the five catalysts. The impedance spectra is fitted using an equivalent circuit consisting of the resistance (electrolyte (R_s), charge transfer (R_{ct})), and constant phase element (C_d). The observed semicircles correspond to the Faradaic charge carrier transfer processes, and their radius signify the charge transfer resistance of the redox processes. According to the fitting results of the equivalent circuit, the charge transfer resistance (R_{ct}) of $\gamma\text{MnOOH@GA/GQDs}$ catalyst is 3715Ω , which is smaller than that of $\gamma\text{MnOOH@GA}$ (4368Ω), $\gamma\text{MnOOH/GQDs}$ (6555Ω) and γMnOOH (15254Ω), but is slightly larger than 20 wt.% Pt/C (2620Ω) catalyst. The $\gamma\text{MnOOH@GA/GQDs}$ hybrid exhibits the smaller charge transfer resistance among the four as-prepared catalysts, which clearly demonstrates that the electrode with $\gamma\text{MnOOH@GA/GQDs}$ allows a much faster transport of electrons during the ORR. The γMnOOH nanotubes has low electrical conductivity, which limits the charge transport on its catalytic active sites. However, the integration of γMnOOH with GA promotes the formation of a porous conducting network with broad pore distribution and large pore diameter, facilitating the charge transfer during the ORR on the γMnOOH surfaces. In addition, the change trend of the catalysts indicates that GQDs play an important role in charge transferring. The surface functionalized GQDs make the γMnOOH nanotubes surface

have more active sites,⁵⁹ which can facilitate the adsorption of oxygen and the binding of reaction intermediates on γ MnOOH surfaces, and therefore enhance the reaction kinetics. The GQDs may work as a surface sensitizer.

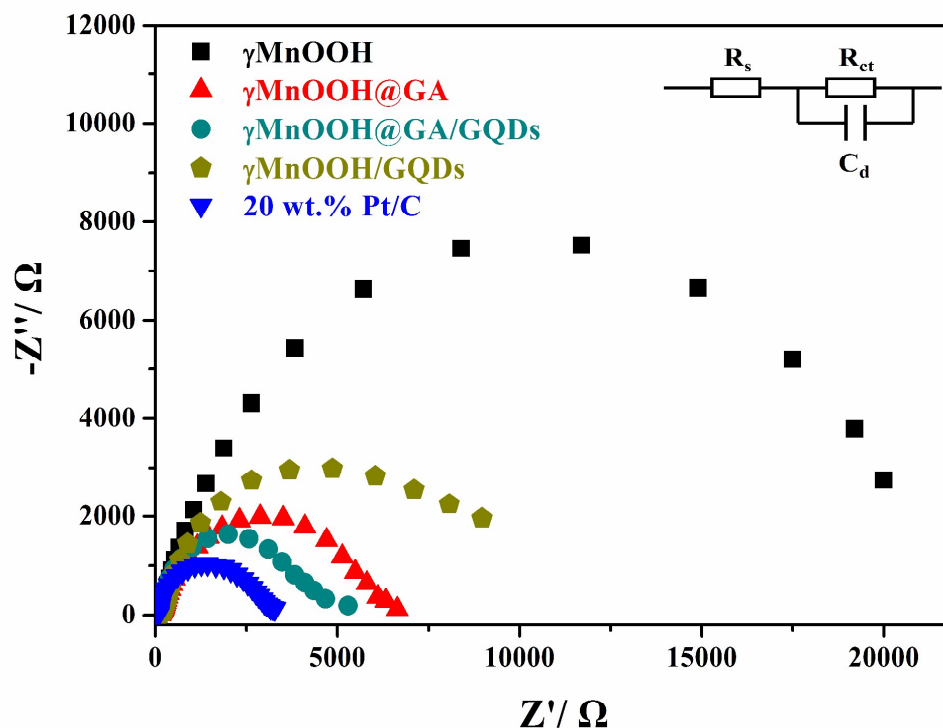


Figure 8. Nyquist plots for γ MnOOH, γ MnOOH@GA, γ MnOOH/GQDs, γ MnOOH@GA/GQDs hybrid, and 20 wt.% Pt/C, respectively.

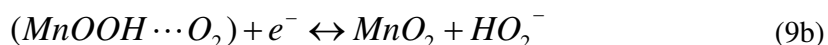
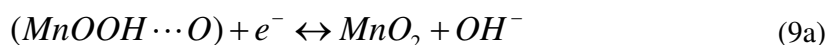
3.3 The reaction pathway of γ MnOOH@GA/GQDs

The γ MnOOH@GA/GQDs catalyst has the similar Tafel slope and the electron number (n) is close to 4, so it favors a direct four electron pathway or a serial 2×2 e pathway for ORR, which can be simply expressed as equation (4), (5), (6) and (7). Supposing that HO_2^- reduction and decomposition proceed (eq 6 and eq 7) infinitely rapidly and completely, the total reactions is equivalent to eq 4. It has been reported that manganese oxides are highly catalytically active toward the peroxide decomposition or disproportionation reaction. Hence the intermediate HO_2^- formed on

γ -MnOOH at the first step can be consumed almost instantaneously.



The redox between Mn species is considered to assist the charge transfer on the basis of the following equations:^{60, 61}



The total reaction of eqs 8a, 9a, and 10 equals to eq 4, which shows a 4e reduction process, whereas the eqs 8b, 9b, and 10 equals to eq 5 with a 2e transfer. These two processes differ in the mode of O₂ adsorption. For reaction 8a, each oxygen molecule may adsorb onto two neighboring MnOOH sites with breaking O=O bond. Our results indicated that both modes coexist in the ORR process because the n is determined to be 3.7 for γ MnOOH@GA/GQDs hybrid. It can facilitate O₂ adsorption, HO₂⁻ decomposition and charge transportation.

4. Conclusion

In conclusion, graphene quantum dots were prepared by electrochemical (EC) procedure and used for modifying 3D graphene aerogel-supported γ -MnOOH

nanotubes. The $\gamma\text{MnOOH}@GA/GQDs$ nanohybrid material has excellent electrocatalytic activity for the ORR in alkaline solution, and favors the four electron pathway to reduce oxygen molecule, which is attributed to the 3D architecture of GA possessing a large specific area, more active sites, and the synergistic effects between GA and γMnOOH . Interestingly, modifying the γMnOOH nanotubes by GQDs brings further advantages in enhancing the ORR electrocatalytic performance. The GQDs may work as a surface sensitizer, which may be ascribed to the structural defects of graphene quantum dots, leading to unique manipulation of the adsorption of O_2 on γMnOOH surfaces. The integration of the individual properties actually enhances the overall performance of the hybrid catalyst. The results indicated that the $\gamma\text{MnOOH}@GA/GQDs$ nanohybrid can be used as a promising low cost and highly efficient cathode catalyst for metal-air batteries. This work may create a new strategy for combining GQDs with other composite nanomaterials as electrocatalysts to further improve ORR activity in metal-air batteries.

Acknowledgements

This study was supported by the National Nature Science Foundation of China (No. 51474255), the Open-End Fund for the Valuable and Precision Instruments of Central South University (No. CSUZC201502).

References

1. M. D. Paster, R. K. Ahluwalia, G. Berry, A. Elgowainy, S. Lasher, K. McKenney and M. Gardiner, *International Journal of Hydrogen Energy*, 2011, **36**, 14534-14551.

2. J. Yuan, J. Wang, Y. She, J. Hu, P. Tao, F. Lv, Z. Lu and Y. Gu, *Journal of Power Sources*, 2014, **263**, 37-45.
3. F. Cheng, Y. Su, J. Liang, Z. Tao and J. Chen, *Chemistry of Materials*, 2010, **22**, 898-905.
4. T.-H. Yang, S. Venkatesan, C.-H. Lien, J.-L. Chang and J.-M. Zen, *Electrochimica Acta*, 2011, **56**, 6205-6210.
5. P. Pei, K. Wang and Z. Ma, *Applied Energy*, 2014, **128**, 315-324.
6. K. Zhang, L. Zhang, X. Chen, X. He, X. Wang, S. Dong, P. Han, C. Zhang, S. Wang, L. Gu and G. Cui, *The Journal of Physical Chemistry C*, 2013, **117**, 858-865.
7. Q. Huang, F. Tao, L. Zou, T. Yuan, Z. Zou, H. Zhang, X. Zhang and H. Yang, *Electrochimica Acta*, 2015, **152**, 140-145.
8. D. Wang, X. Chen, D. G. Evans and W. Yang, *Nanoscale*, 2013, **5**, 5312-5315.
9. P. Trogadas, T. F. Fuller and P. Strasser, *Carbon*, 2014, **75**, 5-42.
10. D. Shin, B. Jeong, B. S. Mun, H. Jeon, H.-J. Shin, J. Baik and J. Lee, *The Journal of Physical Chemistry C*, 2013, **117**, 11619-11624.
11. Z. Jian, P. Liu, F. Li, P. He, X. Guo, M. Chen and H. Zhou, *Angewandte Chemie International Edition*, 2014, **53**, 442-446.
12. Y. L. Cao, H. X. Yang, X. P. Ai and L. F. Xiao, *J Electroanal Chem*, 2003, **557**, 127-134.
13. L. Mao, T. Sotomura, K. Nakatsu, N. Koshiba, D. Zhang and T. Ohsaka, *J Electrochem Soc*, 2002, **149**, A504-A507.
14. K. Matsuki, H. Kamada, *Electrochimica Acta*, 1986, **31**, 13.
15. L. Mao, K. Arihara, T. Sotomura and T. Ohsaka, *Chem Commun*, 2003, **22**, 2818-2819.
16. T. Ohsaka, L. Mao, K. Arihara and T. Sotomura, *Electrochem Commun*, 2004, **6**, 273-277.
17. M. S. El-Deab and T. Ohsaka, *J Electrochem Soc*, 2008, **155**, D14-D21.
18. F. Cheng, J. Shen, W. Ji, Z. Tao and J. Chen, *ACS applied materials & interfaces*, 2009, **1**, 460-466.
19. I. Kruusenberg, M. Marandi, V. Sammelseig and K. Tammeveski, *Electrochemical and Solid-State Letters*, 2009, **12**, F31-F34.
20. C. Li and G. Shi, *Nanoscale*, 2012, **4**, 5549-5563.
21. X. Zhang, Z. Sui, B. Xu, S. Yue, Y. Luo, W. Zhan and B. Liu, *Journal of Materials Chemistry*, 2011, **21**, 6494-6497.
22. S. Sun, P. Wang, S. Wang, Q. Wu and S. Fang, *Materials Letters*, 2015, **145**, 141-144.
23. Y. Zhang, H. Liu, Z. Zhu, K.-w. Wong, R. Mi, J. Mei and W.-m. Lau, *Electrochim Acta*, 2013, **108**, 465-471.
24. X. Zhu, P. Zhang, S. Xu, X. Yan and Q. Xue, *ACS applied materials & interfaces*, 2014, **6**, 11665-11674.
25. J. Shen, Y. Zhu, X. Yang and C. Li, *Chem Commun (Camb)*, 2012, **48**, 3686-3699.
26. Y. Li, Y. Zhao, H. Cheng, Y. Hu, G. Shi, L. Dai and L. Qu, *J Am Chem Soc*, 2012, **134**, 15-18.
27. Y. Dong, C. Chen, X. Zheng, L. Gao, Z. Cui, H. Yang, C. Guo, Y. Chi and C. M. Li, *J Mater Chem*, 2012, **22**, 8764.
28. H. Li, X. He, Z. Kang, H. Huang, Y. Liu, J. Liu, S. Lian, C. H. Tsang, X. Yang and S. T. Lee, *Angew Chem Int Ed Engl*, 2010, **49**, 4430-4434.
29. D. I. Son, B. W. Kwon, D. H. Park, W.-S. Seo, Y. Yi, B. Angadi, C.-L. Lee and W. K. Choi, *Nat Nano*, 2012, **7**, 465-471.

30. J. F. Wang, Y. Chen, C. Liu, D. Ma, *Chem. Commun.*, 2011, **47**, 3502-3504.
31. Y. Dong, W. Tian, S. Ren, R. Dai, Y. Chi and G. Chen, *ACS applied materials & interfaces*, 2014, **6**, 1646-1651.
32. J. Ju and W. Chen, *Anal Chem*, 2015, **87**, 1903-1910.
33. M. Favaro, L. Ferrighi, G. Fazio, L. Colazzo, C. Di Valentin, C. Durante, F. Sedona, A. Gennaro, S. Agnoli and G. Granozzi, *ACS Catalysis*, 2015, **5**, 129-144.
34. Q. Li, S. Zhang, L. Dai and L. S. Li, *J Am Chem Soc*, 2012, **134**, 18932-18935.
35. Y. Song and S. Chen, *ACS applied materials & interfaces*, 2014, **6**, 14050-14060.
36. X. Zhou, Z. Tian, J. Li, H. Ruan, Y. Ma, Z. Yang and Y. Qu, *Nanoscale*, 2014, **6**, 2603-2607.
37. W. Hummers, R. Offeman, *J Am Chem Soc*, 1958, **80**, 1339.
38. Y. Li, Y. Hu, Y. Zhao, G. Shi, L. Deng, Y. Hou and L. Qu, *Adv Mater*, 2011, **23**, 776-780.
39. D. Pan, L. Guo, J. Zhang, C. Xi, Q. Xue, H. Huang, J. Li, Z. Zhang, W. Yu, Z. Chen, Z. Li and M. Wu, *Journal of Materials Chemistry*, 2012, **22**, 3314-3318.
40. J. Peng, W. Gao, B. K. Gupta, Z. Liu, R. Romero-Aburto, L. Ge, L. Song, L. B. Alemany, X. Zhan, G. Gao, S. A. Vithayathil, B. A. Kaiparettu, A. A. Marti, T. Hayashi, J. J. Zhu and P. M. Ajayan, *Nano Lett*, 2012, **12**, 844-849.
41. Y. Meng, W. Song, H. Huang, Z. Ren, S. Y. Chen and S. L. Suib, *Journal of the American Chemical Society*, 2014, **136**, 11452-11464.
42. J. Xiao, L. Wan, X. Wang, Q. Kuang, S. Dong, F. Xiao and S. Wang, *Journal of Materials Chemistry A*, 2014, **2**, 3794-3800.
43. X. Ge, Y. Liu, F. W. Goh, T. S. Hor, Y. Zong, P. Xiao, Z. Zhang, S. H. Lim, B. Li, X. Wang and Z. Liu, *ACS Appl Mater Interfaces*, 2014, **6**, 12684-12691.
44. B. Guo, Q. Liu, E. Chen, H. Zhu, L. Fang and J. R. Gong, *Nano Lett*, 2010, **10**, 4975-4980.
45. Y. F. Lu, S. T. Lo, J. C. Lin, *ACS nano*, 2013, **7**, 6522-6532.
46. F. Zhang, F. Xiao, Z. H. Dong and W. Shi, *Electrochimica Acta*, 2013, **114**, 125-132.
47. J. Zhang and X. S. Zhao, *The Journal of Physical Chemistry C*, 2012, **116**, 5420-5426.
48. S.-B. Ma, K.-Y. Ahn, E.-S. Lee, K.-H. Oh and K.-B. Kim, *Carbon*, 2007, **45**, 375-382.
49. C. Julien, M. Massot, R. Baddour-Hadjean, S. Franger, S. Bach and J. P. Pereira-Ramos, *Solid State Ionics*, 2003, **159**, 345-356.
50. J. Zhou, J. Wang, H. Fang, C. Wu, J. N. Cutler and T. K. Sham, *Chem Commun (Camb)*, 2010, **46**, 2778-2780.
51. Y. Zhang, J. Ge, L. Wang, D. Wang, F. Ding, X. Tao and W. Chen, *Scientific reports*, 2013, **3**, 2771.
52. Y. Tang, H. Qiao, H. Wang and P. Tao, *Journal of Materials Chemistry A*, 2013, **1**, 12512.
53. L. Lai, J. R. Potts, D. Zhan, L. Wang, C. K. Poh, C. Tang, H. Gong, Z. Shen, J. Lin and R. S. Ruoff, *Energy & Environmental Science*, 2012, **5**, 7936.
54. D. Geng, Y. Chen, Y. Chen, Y. Li, R. Li, X. Sun, S. Ye and S. Knights, *Energy & Environmental Science*, 2011, **4**, 760.
55. M. Zhang, Y. Yan, K. Gong, L. Mao, Z. Guo, Y. Chen, *Langmuir*, 2004, **20**, 8781-8785.
56. R. Chen, J. Yan, Y. Liu and J. Li, *The Journal of Physical Chemistry C*, 2015, **119**, 8032-8037.
57. Z. S. Wu, S. Yang, Y. Sun, K. Parvez, X. Feng and K. Mullen, *J Am Chem Soc*, 2012, **134**, 9082-9085.
58. S. Bag, K. Roy, C. S. Gopinath and C. R. Raj, *ACS applied materials & interfaces*, 2014, **6**,

- 2692-2699.
59. L. Wang, C. Lin, D. Huang, F. Zhang, M. Wang and J. Jin, *ACS applied materials & interfaces*, 2014, **6**, 10172-10180.
 60. Ardizzone S, Bianchi C L, Tirelli D, *Colloids and Surfaces A: Physicochemical and Engineering Aspects*, 1998, **134**: 305-312.
 61. Davis D J, Lambert T N, Vigil J A, Rodriguez M A, Brumbach M T, Coker E N, Limmer S J, *The Journal of Physical Chemistry C*, 2014, **118**: 17342-17350.